

# Finite-frequency imaging of the global 410- and 660-km discontinuities using *SS* precursors

Zhen Guo and Ying Zhou

Department of Geosciences, Virginia Tech, Blacksburg, VA 24061, USA. E-mail: [yingz@vt.edu](mailto:yingz@vt.edu)

Accepted 2019 November 27. Received 2019 November 25; in original form 2019 August 12

## SUMMARY

We report finite-frequency imaging of the global 410- and 660-km discontinuities using boundary sensitivity kernels for traveltimes measurements made on *SS* precursors. The application of finite-frequency sensitivity kernels overcomes resolution limits in previous studies associated with large Fresnel zones of *SS* precursors and their interferences with other seismic phases. In this study, we calculate the finite-frequency sensitivities of *SS* waves and their precursors based on a single-scattering (Born) approximation in the framework of travelling-wave mode summation. The global discontinuity surface is parametrized using a set of triangular gridpoints with a lateral spacing of about  $4^\circ$ , and we solve the linear finite-frequency inverse problem (2-D tomography) based on singular value decomposition (SVD). The new global models start to show a number of features that were absent (or weak) in ray-theoretical back-projection models at spherical harmonic degree  $l > 6$ . The thickness of the mantle transition zone correlates well with wave speed perturbations at a global scale, suggesting dominantly thermal origins for the lateral variations in the mantle transition zone. However, an anticorrelation between the topography of the 410-km discontinuity and wave speed variations is not observed at a global scale. Overall, the mantle transition zone is about 2–3 km thicker beneath the continents than in oceanic regions. The new models of the 410- and 660-km discontinuities show better agreement with the finite-frequency study by Lawrence & Shearer than other global models obtained using *SS* precursors. However, significant discrepancies between the two models exist in the Pacific Ocean and major subduction zones at spherical harmonic degree  $>6$ . This indicates the importance of accounting for wave interactions in the calculations of sensitivity kernels as well as the use of finite-frequency sensitivities in data quality control.

**Key words:** Composition and structure of the mantle; Phase transitions; Body waves; Seismic tomography; Wave scattering and diffraction.

## 1 INTRODUCTION

The 410- and 660-km discontinuities have been progressively mapped out in global seismic imaging since the 1990s (Revenaugh & Jordan 1991; Shearer 1991; Flanagan & Shearer 1998; Gu *et al.* 1998, 2003; Lawrence & Shearer 2006; Deuss 2009). High temperature and pressure mineral physics experiments suggest that the two discontinuities are associated with pressure-induced phase transitions of olivine to wadsleyite at about 410 km and ringwoodite to perovskite + magnesiowüstite at about 660 km, respectively (Anderson 1967; Ita & Stixrude 1992). In regional and local seismic imaging, *P*-to-*S* converted waves have been widely used to map the two discontinuities at relatively high resolutions, especially in regions where seismic data have been recorded by small aperture arrays (Shen *et al.* 1998; Li & Yuan 2003; Lee *et al.* 2014; Gao & Liu 2014; Kosarev *et al.* 2017; Kaviani *et al.* 2018; Zhou 2018). In general, global models obtained using *P*-to-*S* converted waves

have lower resolution in oceanic areas because of limited data coverage (Chevrot *et al.* 1999; Lawrence & Shearer 2006). In global studies, the underside reflections of *SS* waves (*SS* precursors) have been used to map the global depth perturbations of the 410 and the 660. *SS* precursors are most sensitive to discontinuity structures near the *SS* wave bounce points and therefore they provide better global coverage than *P*-to-*S* converted waves, especially in oceanic regions where very few seismic stations are deployed.

*SS* precursors are secondary waves reflected at the underside of the 410-km and the 660-km discontinuities, their amplitudes are relatively small due to the low impedance ratio across the two seismic discontinuities (Fig. 1). Previous *SS* precursor studies in imaging the global mantle transition zone structures commonly chose to stack the *SS* precursors in large circular bins to improve the signal-to-noise ratios and obtain depth perturbations on the discontinuities based on the conventional JWKB ray theory (Shearer 1991; Gu *et al.* 1998, 2003; Schmerr & Garnero 2006; Houser *et al.* 2008; Deuss 2009).

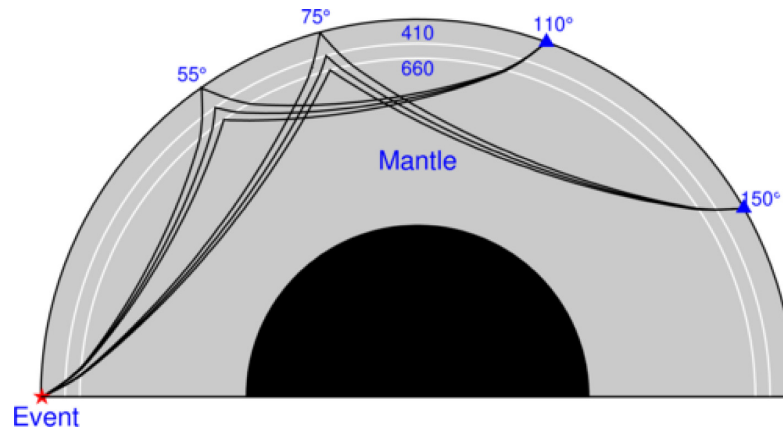


**Figure 1.** Ray paths of *SS*, *S410S* and *S660S* waves at epicentral distances of  $110^\circ$  and  $150^\circ$ . The star and triangles indicate locations of the earthquake event and the recording stations, respectively.

Ray theory is a high-frequency approximation which assumes that seismic waves travel through the earth along infinitesimally narrow paths. In reality, however, seismic waves have finite frequency and *SS* waves are sensitive to a large area on the boundary centered at the bounce point. It has been suggested by several studies that topographic structures with sizes smaller than the first Fresnel zone may not be resolved properly using the traditional ray theory (Neele *et al.* 1997). The resolution of the ray-theoretical models is limited by the large Fresnel zone of *SS* waves and their precursors ( $\sim 1000$  km at 20-s period) and only large-scale features are reliable. A better theory, which can account for scattering, wave front healing and other finite frequency effects of seismic waves is needed to improve the resolution of smaller scale topographic anomalies. Neele & de Regt (1999) proposed a method to approximate the finite-frequency sensitivities of *SS* and *PP* precursors over the first Fresnel zone. They applied the method to a large synthetic data set and showed that depth variations with a lateral scale smaller than the first Fresnel zone but larger than the dominant wavelength can be well resolved. The first global topographic maps of the 410 and the 660 based on finite-frequency theory were published by Lawrence & Shearer (2008) using traveltimes sensitivity kernels of *SS* precursors calculated based on ray tracing (Dahlen 2005). The power spectra of the seismic phases in the reference model were approximated by the observed power spectra, and, the sensitivity kernels were stacked in circular bins of different sizes in the inversions.

In this study, we construct a global data set of finite-frequency traveltimes measurements of *SS* waves and *SS* precursors by measuring traveltimes differences between the observed and synthetic seismograms in the frequency domain. One major concern in imaging the 410 and the 660 using *SS* precursors is phase interactions (e.g. precursors of *ScSScS* wave and the postcursors of  $S_{\text{diff}}$  interfere with *SS* precursors). To reduce possible uncertainties in *SS* precursor data, earlier studies often chose to limit the range of epicentral distance to avoid possible phase interference, which limits the spatial resolution of available data (Schmerr & Garnero 2006; Deuss 2009; Lessing *et al.* 2014). To overcome the above limitations, we calculate sensitivity kernels in the framework of travelling-wave mode coupling, which fully accounts for interference of seismic waves arriving in the measurement windows, the effects of source radiation and seismogram windowing/tapering. This study is the first study to image the 410- and 660-km discontinuities using single-trace *SS* (and precursor) traveltimes measurements and individual finite-frequency sensitivity kernels.

The sensitivity kernels can be used to identify measurements that are heavily influenced by shallower multiples, and, those measurements can be excluded when they are not most sensitive to the depth perturbations of the 410 and the 660. We will focus on finite-frequency effects in the imaging of the 410 and the 660 using single trace traveltimes measurements of *SS* precursors by investigating models obtained using 2-D diffractive tomography and those obtained from ray-theoretical back-projections using the same data set. We compare our finite-frequency discontinuity model with previous studies and show that the new model agrees better with the finite-frequency model by Lawrence & Shearer (2008) than other global models imaged using *SS* precursors based on ray theory. We will discuss major discrepancies between the two finite-frequency models and the significance of data processing in finite-frequency imaging.

## 2 FINITE-FREQUENCY TRAVELTIME MEASUREMENTS

We built a global data set of the finite-frequency traveltimes measurements using seismograms recorded at 150 stations in the Global Seismological Network (GSN) for earthquakes that occurred between January 2003 and September 2014 (Fig. 2). The earthquakes have moment magnitudes ranging from 6.0 to 8.5 and focus depths less than 100 km. All available seismograms with epicentral distances between  $90^\circ$  and  $160^\circ$  are downloaded from the Data Management Center at the Incorporated Research Institutions for Seismology (IRIS). Initial data processing includes removing instrument responses, rotating the horizontal components to obtain the transverse component seismograms and applying bandpass filter with corner frequencies at 0.01 and 0.1 Hz. We visually inspected seismograms and carefully selected the ones with high signal-to-noise ratios and clear *SS* waves and precursors. We corrected abnormal polarities of the transverse component seismograms at several stations and we discarded seismograms with highly deformed *SS* waveforms. The final data set contains a total number of about 6400 seismograms from 1117 earthquakes.

Synthetic seismograms are calculated in a 1-D reference earth model IASP91 (Kennett & Engdahl 1991) based on travelling-wave mode summation up to 0.2 Hz (Liu & Zhou 2016). The global centroid-moment-tensor (CMT) solution and the USGS Preliminary Determination of Epicenters (PDE) source locations and origin times are used in the calculations of the 1-D synthetic seismograms.

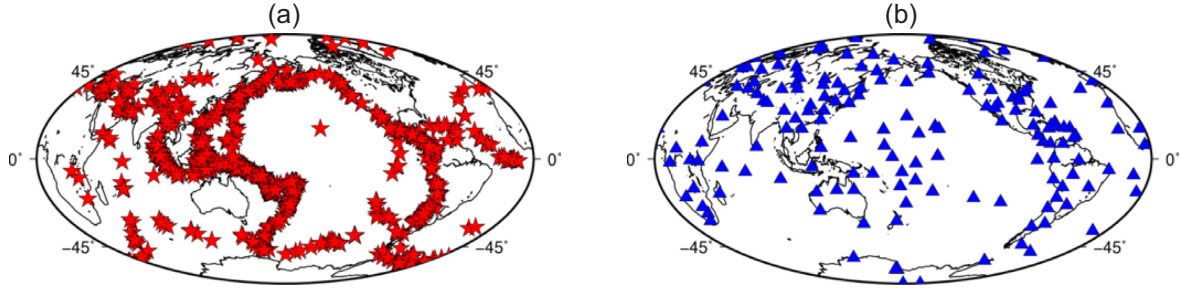


**Figure 2.** (a) Distribution of 1117 teleseismic earthquakes ( $6.0 < M_w < 8.5$ ) used in this study. The epicentral distance of the data set ranges from  $90^\circ$  to  $160^\circ$ . (b) Locations of 150 GSN stations used in this study.

The same bandpass filter is applied to the synthetic seismograms. We manually pick measurement windows centered near the maximum amplitudes of the phases (*SS* or *SS* precursors) and the length of the measurement time windows ranges from 70 to 120 s. Finite-frequency traveltimes measurements are made with a cosine taper of the same length to limit spectra leakage (Fig. 3). The spectrum of the cosine taper shows a relatively broad central peak and very weak side lobes (Deng & Zhou 2015). The differences in traveltimes between the synthetic and observed signals are calculated in the frequency domain (Xue *et al.* 2015).

Fig. 3 shows examples of observed and synthetic seismograms from the data set. The observed seismogram in (c) is recorded at station EFI on East Falkland Island from a moment magnitude 6.9 earthquake in Indonesia, and the observed seismogram in (d) is recorded at station LBTB from a moment magnitude 7.5 earthquake in Mexico. The epicentral distances are  $130^\circ$  and  $133^\circ$ , respectively. Time windows used for measuring the traveltimes residuals of *SS* waves and *SS* precursors are shaded on the seismograms. It is important to point out that finite-frequency traveltimes measurements depend on the length and position of the measurement windows as well as the time-domain taper applied in making the measurements. The effects of windowing and tapering are accounted for in the calculation of the finite-frequency sensitivity of each measurement. In this paper, we will focus on inversions using data obtained at a measurement period of 20 s.

### 3 FINITE-FREQUENCY SENSITIVITIES TO BOUNDARY PERTURBATIONS

Depth perturbations on seismic discontinuities will cause arrival time anomalies of *SS* waves and *SS* precursors. The differences in arrival times between the observed and synthetic seismic phases can be used to image lateral variations of the seismic discontinuities with respect to a 1-D reference earth model. Theoretically, the traveltimes difference between an observed and a synthetic *SdS* wave (*S410S* or *S660S*),  $\delta t_{SdS}$ , can be written as a 2-D integration over the global surface of the corresponding discontinuity  $\Sigma$  (the 410-km or the 660-km discontinuity),

$$\delta t_{SdS}(\omega) = \iint_{\Sigma} K_{\Sigma}^{SdS}(\mathbf{x}, \omega) \delta d(\mathbf{x}) d\Sigma, \quad (1)$$

where  $K_{\Sigma}^{SdS}(\mathbf{x}, \omega)$  is the sensitivity of an individual *SS* precursor (*SdS*) traveltimes measurement at an angular frequency  $\omega$  to depth perturbations  $\delta d(\mathbf{x})$  of the discontinuity  $\Sigma$ , and  $\mathbf{x}$  is the position vector. In ray theory, seismic waves propagate as rays along infinitesimally narrow paths following *Snell's* law. Therefore, the arrival time perturbation of an *SS* precursor depends only on the discontinuity depth perturbation at the bounce point. Eq. (1) then becomes

a simple product of the 1-D time-depth derivative and the depth perturbation at the bounce point (Gu & Dziewonski 2002). In finite frequency theory, seismic waves experience scattering, wave front healing and other diffractive effects during wave propagation. Therefore, the traveltimes of *SS* precursors are not only sensitive to the structure at the bounce point but also to structures within a broad area centered at the bounce point on the discontinuity. In this paper, we calculate the finite-frequency sensitivity  $K_{\Sigma}^{SdS}(\mathbf{x}, \omega)$  based on single-scattering (Born) approximation in the frame work of travelling wave mode coupling,

$$K_{\Sigma}^{SdS}(\mathbf{x}, \omega) = \text{Im} \left[ \omega^{-1} \frac{[\mathcal{K}_{\Sigma}(\mathbf{x}, \omega) \otimes h(\omega)] [s(\omega) \otimes h(\omega)]^*}{[s(\omega) \otimes h(\omega)] [s(\omega) \otimes h(\omega)]^*} \right], \quad (2)$$

where  $s(\omega)$  is the displacement spectrum in the reference earth model and  $h(\omega)$  is the spectrum of the cosine taper used in making the measurement. The operator  $\otimes$  denotes convolution in frequency domain and the asterisk denotes the complex conjugate. The complex waveform kernel for boundary depth perturbations  $\mathcal{K}_{\Sigma}(\mathbf{x}, \omega)$  is

$$\begin{aligned} \mathcal{K}_{\Sigma}(\mathbf{x}, \omega) = & \sum_{\sigma'} \sum_{\sigma''} S' \left[ \frac{e^{-i(k' \Delta' + \pi/4)}}{\sqrt{8\pi k' |\sin \Delta'|}} \right] \\ & \times \left[ \frac{e^{-i(k'' \Delta'' + \pi/4)}}{\sqrt{8\pi k'' |\sin \Delta''|}} \right] R'' \\ & \times [\Omega^{(1)} + \Omega^{(2)}]_{-}^{+}. \end{aligned} \quad (3)$$

In the above equation, the single prime and double primes represent quantities calculated along the great circle path from the source to the scatterer (mode  $\sigma'$ ) and the scatterer to the receiver (mode  $\sigma''$ ), respectively.  $\Delta$  is the great circle distance between the source and receiver and  $k$  is the wavenumber. The source and receiver terms are  $S'$  and  $R'$ , respectively and  $\Omega^{(1)}$  and  $\Omega^{(2)}$  are boundary scattering coefficients. Detailed expressions of the source and receiver terms as well as scattering coefficients can be found in Zhou *et al.* (2005).

For *SS* waves, traveltimes delays caused by depth perturbations on the seismic discontinuity  $\Sigma$  can be expressed as

$$\delta t_{SS}(\omega) = \iint_{\Sigma} K_{\Sigma}^{SS}(\mathbf{x}, \omega) \delta d(\mathbf{x}) d\Sigma, \quad (4)$$

where  $K_{\Sigma}^{SS}(\mathbf{x}, \omega)$  is the *SS* wave sensitivity to the depth perturbations on the boundary  $\Sigma$ . Eqs (1) and (4) shows a linear relation between the traveltimes measurements and boundary depth perturbations, which leads to a simple expression for *SdS*-*SS* differential measurements

$$\delta t_{SdS}(\omega) - \delta t_{SS}(\omega) = \iint_{\Sigma} [K_{\Sigma}^{SdS}(\mathbf{x}, \omega) - K_{\Sigma}^{SS}(\mathbf{x}, \omega)] \times \delta d(\mathbf{x}) d\Sigma. \quad (5)$$

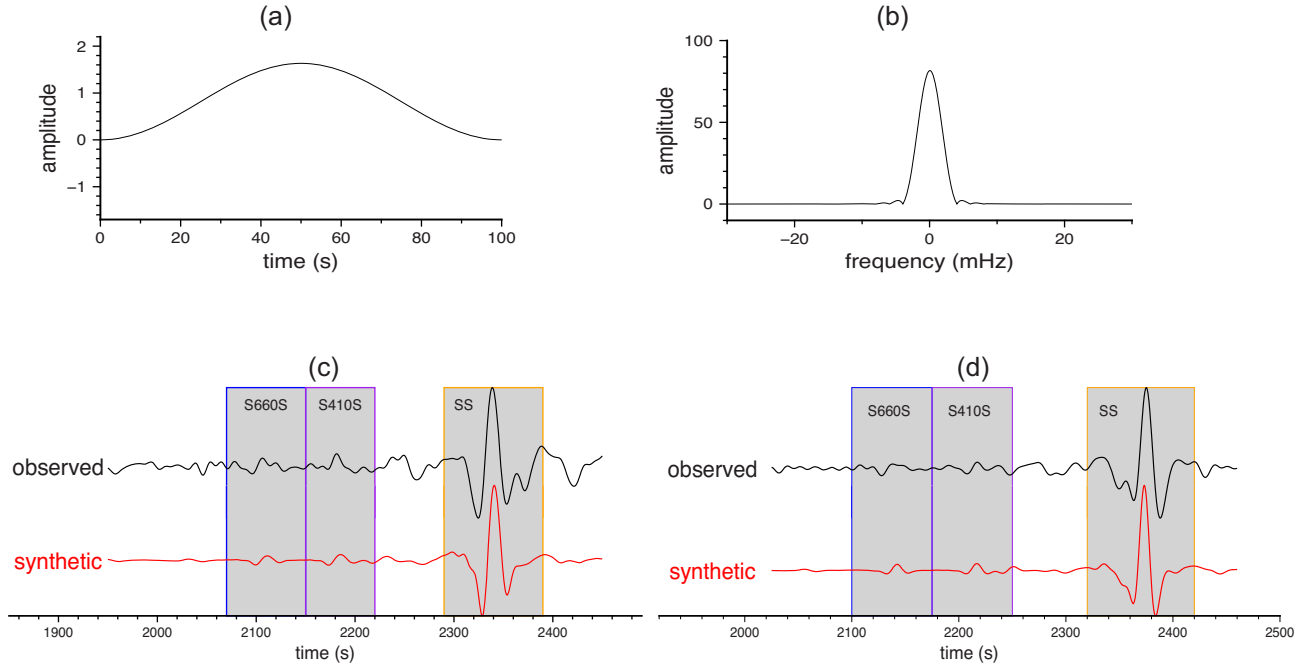


**Figure 3.** Panels (a) and (b) are a 100-s cosine taper in the time domain and its spectrum in the frequency domain, respectively. Panels (c) and (d) are example observed and synthetic seismograms with clear SS, S410S and S660S waves, recorded at station EFI for an Indonesia earthquake occurred on 26 May 2003 ( $M_w = 6.9$ ) and at station LBTB for a Mexico earthquake occurred on 22 January 2003 ( $M_w = 7.5$ ), respectively. The shaded areas indicate time windows used for traveltime measurements.

We calculate finite-frequency sensitivity kernels for SS waves and their precursors ( $K_{\Sigma}^{SS}$  and  $K_{\Sigma}^{SdS}$ ) in a 1-D reference earth model IASP91, fully accounting for phase interactions, source radiation patterns, time-domain windowing and tapering applied in making frequency-dependent traveltime measurements (Zhou *et al.* 2005; Zhou 2009; Deng & Zhou 2015).

Fig. 4 shows examples of 2-D traveltime sensitivity of S410S and S660S waves to depth perturbations of the 410- and 660-km discontinuities. The epicentral distance is  $133^\circ$  and the kernels are calculated for traveltime measurements at a period of 20 s. The sensitivity kernels show the typical X shape with maximum positive values in the center of the X and alternating side bands in the second and third Fresnel zones. The size of the first Fresnel zone (with positive sensitivity) is about  $15^\circ \times 15^\circ$ , indicating that ray theory, which assumes traveltime sensitive only to structure at the bounce point, is a rather crude approximation in this case.

In general, the boundary sensitivity of SS waves is about an order of magnitude smaller than the sensitivity of SdS waves (Fig. 5). Therefore, the sensitivity kernels of the SdS–SS differential measurements show only minor differences from the SdS sensitivity kernels. We point out that the boundary sensitivity kernels are associated with measurement time windows, which may include multiple phases arriving closely in time. Therefore, they often have structures more complex than those plotted in Figs 4 and 5 due to interfering seismic phases. For those measurements, the typical X-shape structure due to the minimum-maximum nature of the precursors will be deformed and the amplitudes of the sensitivity may become extreme. The complexity of the finite-frequency sensitivity kernels can be used to identify measurements associated with wave interference due to multiples of a shallower interface or other seismic phases. We exclude those measurements as linear perturbation theory may not apply when the reference phase is much weaker than scattered waves.

#### 4 THE INVERSE PROBLEM

We parametrize the surface of the Earth using a set of spherical triangular gridpoints. The spherical triangles are 16-fold, with 2562 vertexes and a lateral spacing of about  $4.3^\circ$  (Zhou *et al.* 2005). With this model parametrization, the matrix form of the inverse problem in eq. (1) can be expressed as

$$\mathbf{Ax} = \mathbf{b}, \quad (6)$$

where  $\mathbf{x}$  is the model vector of unknown depth perturbations on the discontinuity and  $\mathbf{b}$  is the data vector of SdS–SS traveltime residuals.  $\mathbf{A}$  is the sensitivity matrix with components  $a_{ij}$  representing the sensitivity of the  $i$ th observed data to the depth perturbation at the  $j$ th model grid.

Due to uneven data coverage and the presence of noise, the inverse problem is ill-posed and regularization is required to find an optimal solution. We apply a Tikhonov regularization to eq. (6) and solve a regularized least-squares inverse problem

$$(\mathbf{A}^T \mathbf{A} + \alpha^2 \mathbf{I}) \mathbf{x} = \mathbf{A}^T \mathbf{b}, \quad (7)$$

where  $\alpha$  is the Tikhonov regularization parameter, and  $\mathbf{I}$  is an identity matrix.

To solve the above inverse problem, matrix  $\mathbf{A}$  is decomposed using singular value decomposition (SVD),

$$\mathbf{A} = \mathbf{U} \mathbf{\Sigma} \mathbf{V}^T, \quad (8)$$

where  $\mathbf{u}_i$  in  $\mathbf{U}$  and  $\mathbf{v}_i$  in  $\mathbf{V}$  are the left and right singular vectors, respectively, and the matrix  $\mathbf{\Sigma}$  is a diagonal matrix containing the singular values  $\sigma_i$ .

The Tikhonov solution to the least-square problem is then written as

$$\mathbf{x} = \sum_i \frac{\sigma_i^2}{\sigma_i^2 + \alpha_i^2} \frac{\mathbf{u}_i^T \mathbf{b}}{\sigma_i} \mathbf{v}_i. \quad (9)$$

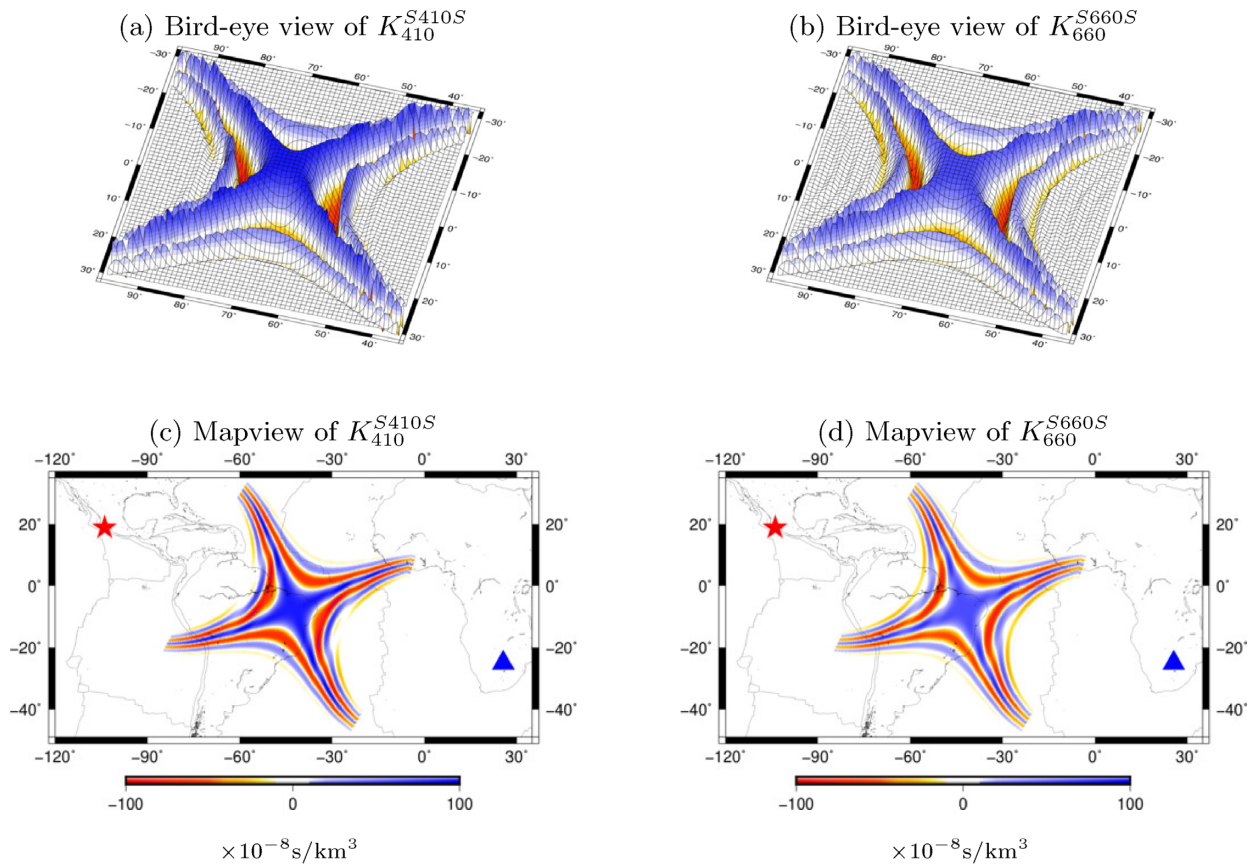


**Figure 4.** (a) Bird-eye view of example finite-frequency sensitivity of an  $S_{410S}$  wave at a period of 20 s to depth perturbations of the 410-km discontinuity. The epicentral distance is  $133^\circ$  and the mapview of the sensitivity kernel is plotted in (c) where the earthquake (star) is located off the west coast of Mexico and the station LBTB (triangle) is in Africa. The sensitivity of the corresponding  $S_{660S}$  to depth perturbations on the 660-km discontinuity is plotted in (b) and (d).

The choice of the regularization parameter  $\alpha$  is made by studying the trade-offs between the model norm and data misfit. Typically, the optimal value of the regularizing parameter is chosen near the lower left corner of the trade-off curve where further reduction in model norm starts to introduce a large increase in data misfit.

## 5 FINITE-FREQUENCY EFFECTS IN DISCONTINUITY IMAGING

The 410- and 660-km discontinuity models obtained from finite-frequency inversions are plotted in Fig. 6. We have removed the mean perturbations of the two discontinuities and the reference depths of the 410-km and the 660-km discontinuities in Fig. 6 are 411.6 and 660.4 km, respectively. Positive perturbations (in blue) indicate discontinuity depths greater than the reference depths, and negative perturbations (in red) indicate shallower discontinuity. Overall, the 660-km discontinuity shows larger depth variations than the 410-km discontinuity, which is consistent with traveltimes observations. The  $S_{660S}$  and  $S_{410S}$  measurements have similar standard deviations (6.14 and 6.10 s, respectively) while the same amount of depth perturbations on the two discontinuities would predict larger traveltimes anomalies in the  $S_{410S}$  waves than the  $S_{660S}$  waves. Stronger topographic variations of the 660-km discontinuity have also been observed in several previous studies (Flanagan & Shearer 1998; Gu *et al.* 2003; Lawrence & Shearer 2008).

The 660-km discontinuity is overall shallower in oceanic regions and deeper in a broad region across the Eurasia and along the

west coast of the North America. Regional studies using receiver functions and PP/SS precursors have reported similar depressed 660 topography in the Sea of Okhotsk, Eastern Russia, Northeastern China as well as the North American Farallon subduction zone (Heit *et al.* 2010; Schmerr & Thomas 2011; Gao & Liu 2014; Zheng *et al.* 2015; Wang & Pavlis 2016; Zhou 2018). The 660-km discontinuity beneath the Mediterranean Sea and the Middle East shows several small-scale depressions which were also imaged by Kaviani *et al.* (2018).

The ocean–continent contrast is much weaker on the 410-km discontinuity. There is an apparent age-dependent signature in the Pacific Ocean, where the 410 becomes deeper towards the middle ocean spreading centers. The 410-km discontinuity is depressed in the western North America and eastern Asia extending from Tibet through central and northern China to the western Sea of Okhotsk, in general agreement with regional studies (Heit *et al.* 2010; Gao & Liu 2014; Wang & Pavlis 2016).

In Fig. 6, we compare the finite-frequency models of the 410- and 660-km discontinuities with depth perturbations obtained from back-projection using the same  $SdS$ – $SS$  traveltimes measurements. In ray-theoretical data back projection, we do not invert the traveltimes measurements but estimate discontinuity depth perturbations from traveltimes residuals using 1-D time–depth derivatives. The depth perturbations are averaged in a moving circular cap with a constant radius and plotted in Fig. 7. When the cap size is small ( $4^\circ$ ), the resulting back-projection maps become more noisy due to rather small number of data points available in the averaging cap, especially in South America and Western Australia

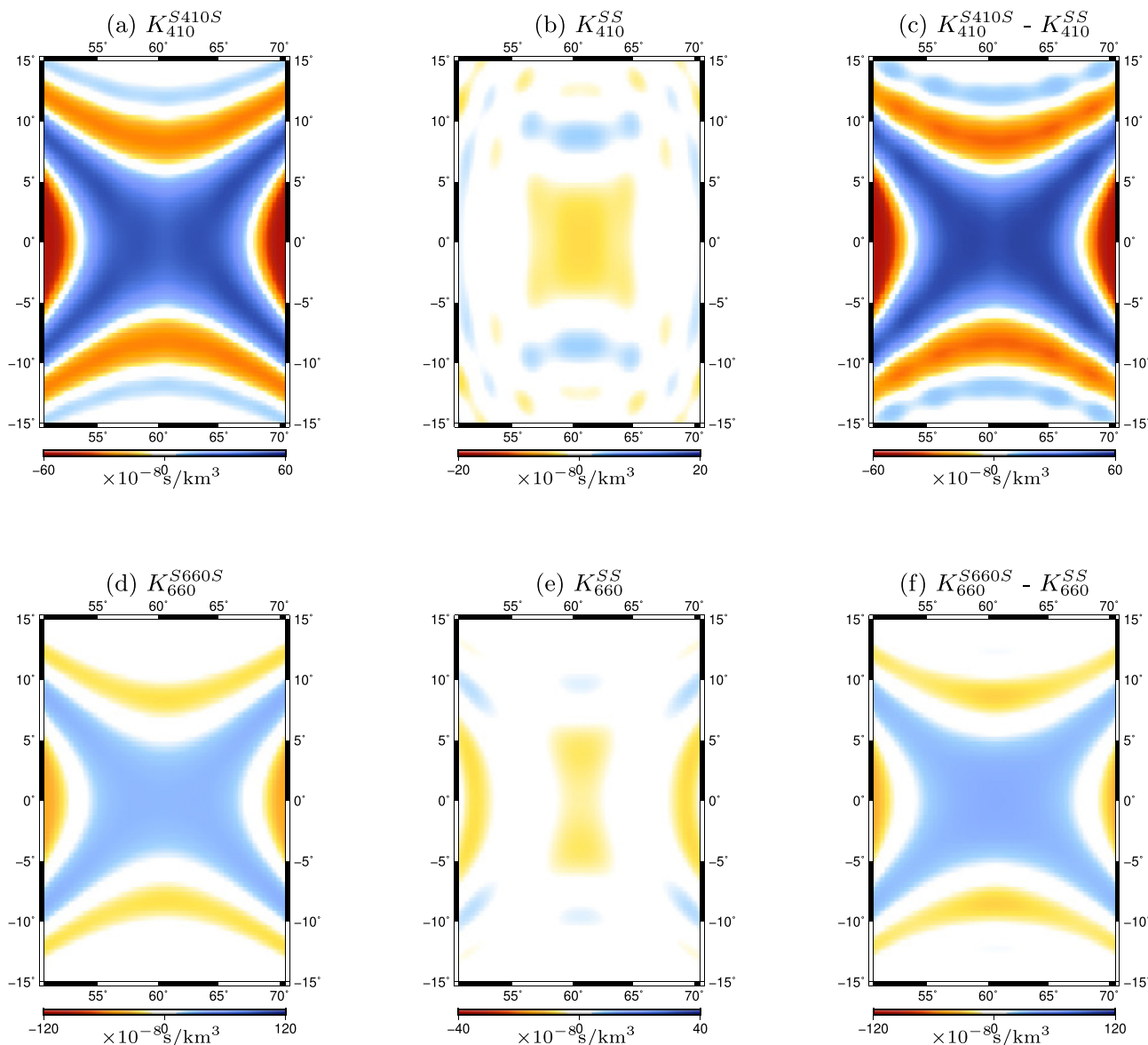


**Figure 5.** Zoom-in view of sensitivity kernels of S410S, S660S and SS waves recorded at station BJT (longitude = 116.17°, latitude = 40.02°) with an epicentral distance of 120° from a  $M_w$  6.3 earthquake in Puerto Rico area. The SS sensitivities are much smaller in magnitude and plotted on difference color scales. SdS and SS waves have different sensitivity polarity as a depression of the 410-km (or 660-km) discontinuity will speed up SdS waves but slow down SS waves, and vice versa for an uplift.

where data sampling is sparse. For example, extreme values in isolated regions in South America and Eastern North America in Fig. 6(c) are a result of unsuppressed noise in data due to insufficient averaging. When the radius of the cap is 6°, the structure becomes more smooth. Overall, the long-wavelength structures of the 410- and 660-km discontinuity maps obtained using ray-theoretical data back projection agree well with finite-frequency models.

In Fig. 7, the finite-frequency sensitivity density and the back-projection ray density show similar coverage and smoothness when the size of the circular cap used in ray-theoretical back projection is 6°. The resulting models show large discrepancies in their dominant structure length scales (Fig. 6). The finite-frequency models show much stronger small-scale structures that are absent in the ray-theoretical back-projection models. In regions where data

coverage is sparse, depth perturbations are very small, indicating that the finite-frequency models have been adequately damped (Figs 7 and A1). The stronger small-scale structures are expected as finite-frequency sensitivity kernels account for wave diffractive effects. For example, the anomalies along the western North America are much narrower and mostly confined in the continent regions while anomalies are much broader and diffused in the ray-theoretical back-projection models, regardless of the cap size.

We calculate the correlation coefficients between the finite-frequency models and the back-projection models as a function of spherical harmonic degree up to  $l = 20$  in Fig. 8. Models obtained using finite-frequency tomography and ray-theoretical back projection are positively correlated at all spherical harmonic degrees, regardless of the averaging cap size. The two 410-km discontinuity

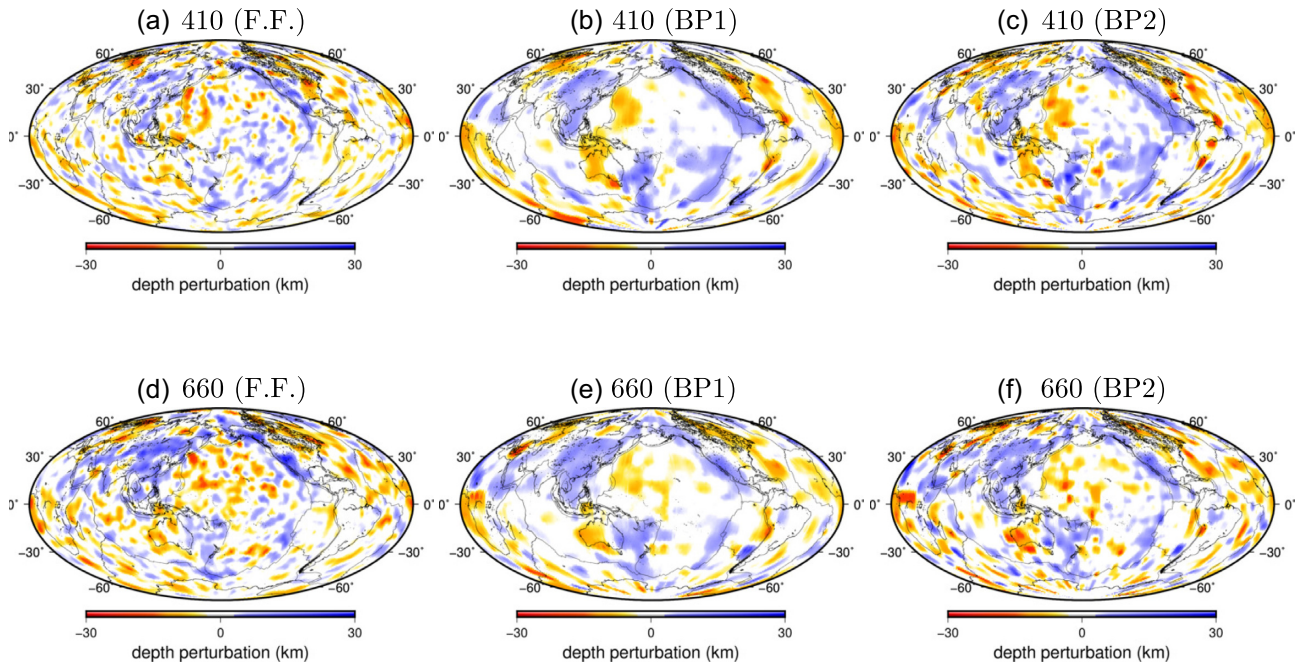


**Figure 6.** Finite-frequency effects in imaging depth perturbations of the 410-km and the 660-km discontinuities. Panel (a) depth perturbations of the 410-km discontinuity inverted from  $SdS$ - $SS$  traveltimes measurements using finite-frequency sensitivity kernels. Panels (b) and (c) are ray-theoretical back-projection models where perturbations are averaged in a moving circular cap with a radius of  $6^\circ$  (BP1) and  $4^\circ$  (BP2). Panels (d)–(f) are the finite-frequency and ray-theoretical back-project models for depth perturbations on the 660-km discontinuity. The finite-frequency model and ray-theoretical back-project models are obtained using the same traveltimes data without crustal and mantle wave speed corrections.

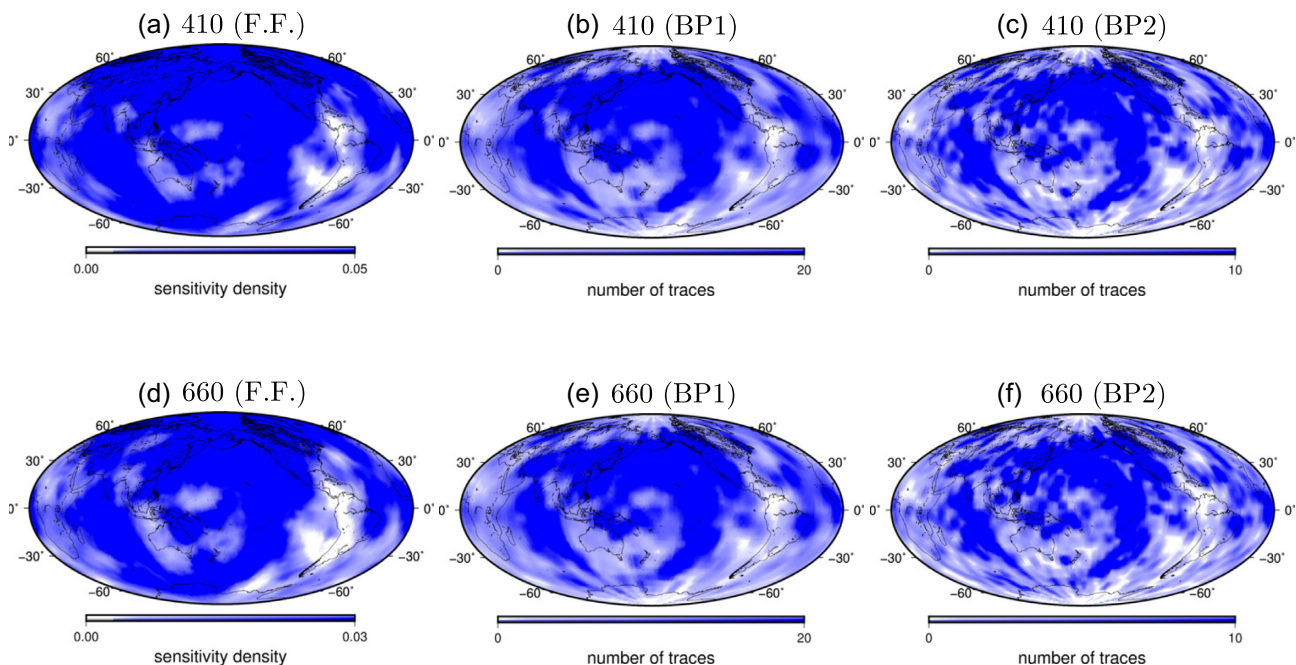


**Figure 7.** Panel (a) is the sensitivity density (diagonal elements of the matrix  $A^T A$ ) in finite-frequency tomography of the 410-km discontinuity. Panels (b) and (c) are the number of traces per circular cap in the back-projection models BP1 and BP2, respectively. Panels (d)–(f) are the same as (a)–(c) but for the 660-km discontinuity models in Fig. 6.

models are well correlated with a correlation coefficient of 0.96 in their large-scale structures ( $l < 5$ ), and the correlation coefficient decreases to  $\sim 0.8$  at intermediate length scales ( $6 \leq l \leq 14$ ). For smaller scale structure with harmonic degree  $l \geq 15$  (wavelength  $< \sim 2500$  km), the correlation coefficient decreases to  $\sim 0.5$ . The

correlation between the two 660-km discontinuity models show very similar variations as a function of spherical harmonic degree, except that small-scale structures show better correlations with the finite-frequency model when a  $4^\circ$  cap is used in the back-projection model.

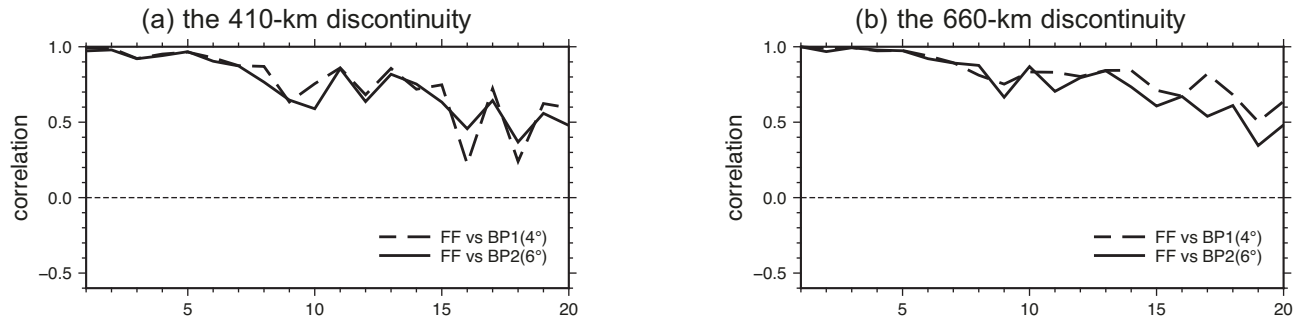


**Figure 8.** (a) Correlation coefficient as a function of spherical harmonic degree between the finite-frequency 410-km discontinuity model and the two back-projection models in Fig. 6. (b) Same as (a) but for the 660-km discontinuity models.

## 6 CRUST AND MANTLE CORRECTIONS

Lateral variations in crustal structure and seismic wave speed in the upper mantle will introduce traveltime differences between observed and synthetic seismograms calculated in the 1-D reference earth model, IASP91 (Kennett & Engdahl 1991). These traveltime anomalies can be subtracted from  $SS$  and  $SdS$  measurements by applying corrections using published 3-D crust and mantle velocity models. In this section, we investigate the impact of crustal and mantle corrections on the imaging of the 410- and 660-km discontinuities in finite-frequency tomography. We calculate expected traveltime anomalies caused by the 3-D structure of the crust using a global crustal model CRUST1.0 (Laske *et al.* 2013). This is a  $1^\circ \times 1^\circ$  model which parametrized wave speeds and density in the crust and uppermost mantle as 8 layers in every  $1^\circ \times 1^\circ$  cell. Crustal corrections are positive beneath continents and negative in oceanic areas. The maximum correction is about 4.6 s for  $SS$  waves with bounce points in the Tibetan Plateau where the crust is about 60 km thicker than in the reference model.

Mantle wave speed corrections are often applied to account for traveltime anomalies caused by 3-D wave speed structure in the mantle using global models from independent studies. This method has been suggested to be more straightforward and accurate in  $SS$  precursor imaging than joint inversions to resolve discontinuity depth variations and wave speed perturbations simultaneously (Houser *et al.* 2008). This is because data sets required to image discontinuity depths are different from those that constrain seismic wave speed in the bulk mantle, including surface waves, body waves and free oscillations (Panning & Romanowicz 2006; Zhou *et al.* 2006; Ritsema *et al.* 2011; Schaeffer & Levedev 2013; Moulik & Ekstrom 2014). We calculate traveltime corrections using two different global 3-D mantle models, S40RTS (Ritsema *et al.* 2011) and S362ANI+M (Moulik & Ekstrom 2014). In model S40RTS, wave speed perturbations are with respect to a 1-D reference earth model PREM (Dziewonski & Anderson 1981) while the 3-D model S362ANI+M is anisotropic and wave speed perturbations are deviations from a 1-D reference model STW105 (Kustowski *et al.* 2008). Wave propagation simulations in 3-D earth models using the spectral element method have shown that traveltime corrections based on ray theory are adequate for wave speed models obtained using ray theory (Deng & Zhou 2015), we calculate wave speed perturbations in S40RTS and S362ANI+M with respect to the same 1-D reference model IASP91 and then integrate traveltime anomalies along the ray paths of  $SS$  waves and  $SS$  precursors. In general, wave speed corrections for  $SdS$ – $SS$  measurements are smaller than that for individual  $SS$  and  $SdS$  waves, which is not unexpected as wave speed

structure in the lower mantle introduces similar shifts in both the  $SS$  and  $SdS$  traveltimes.

The absolute traveltime corrections are significant with maximum values up to 15–20 seconds for some paths, but the corrections do not change the general geographic pattern of the  $SdS$ – $SS$  traveltime residuals when plotted at the  $SS$ -wave bounce points (Fig. 9). However, the corrections do affect the amplitudes and the exact locations of the discontinuity anomalies in the final models (Fig. 10). For example, the age-dependent depth perturbation of the 410-km discontinuity in the Pacific Ocean in Fig. 6 becomes much weaker after wave speed corrections are applied. In addition to oceanic regions, crustal and mantle corrections also have an impact on discontinuity structures beneath stable cratons (e.g. the Canadian shield and the Baltic Shield) where the magnitude of  $SdS$ – $SS$  traveltime measurements is either reduced or changes polarity after crustal and mantle wave speed corrections (Fig. 10). This can be explained by early arrivals of  $SS$  waves associated with increased wave speed in the upper mantle in those regions. The strong discontinuity anomalies beneath California also become much weaker after the corrections are applied. It is noteworthy that traveltime corrections made using different global mantle wave speed models (S40RTS versus S362ANI) are highly correlated and the final models after wave speed corrections do not show major differences (Figs 10 and 11).

The impact of crustal and mantle wave speed corrections on discontinuity structures at different length scales are plotted in Fig. 11. In spherical harmonic analysis, the power spectra is expected to decrease rapidly with angular degree when the peak amplitude of lateral variations remains the same. For example, the spectra power at degree  $l = 2$  is about one order of magnitude larger than the spectra power at degree  $l = 12$  when depth perturbations at the two harmonics degrees have the same peak amplitude. In general, crustal and mantle corrections emphasize low spherical harmonic degree structures in the discontinuity maps (Figs 10 and 11). For example, the maximum spectra power of the 660-km discontinuity map is at degree  $l = 2$  without data corrections, while the degree-one ( $l = 1$ ) structure becomes the strongest after crustal and mantle wave speed corrections are applied. This leads to low correlation coefficients between models obtained with and without corrections at degrees 1–2. The correlation is positive but weak at degrees  $l = 4$ – $5$  and increases with spherical harmonic degree with strongest correlations at degrees  $l \geq 8$  (length scale  $\leq 2500$  km). The thickness of the mantle transition zone is least sensitive to crust and mantle wave speed corrections and is strongly correlated between models with and without the corrections. Overall, the discontinuity models with and without crust and mantle wave speed corrections are well

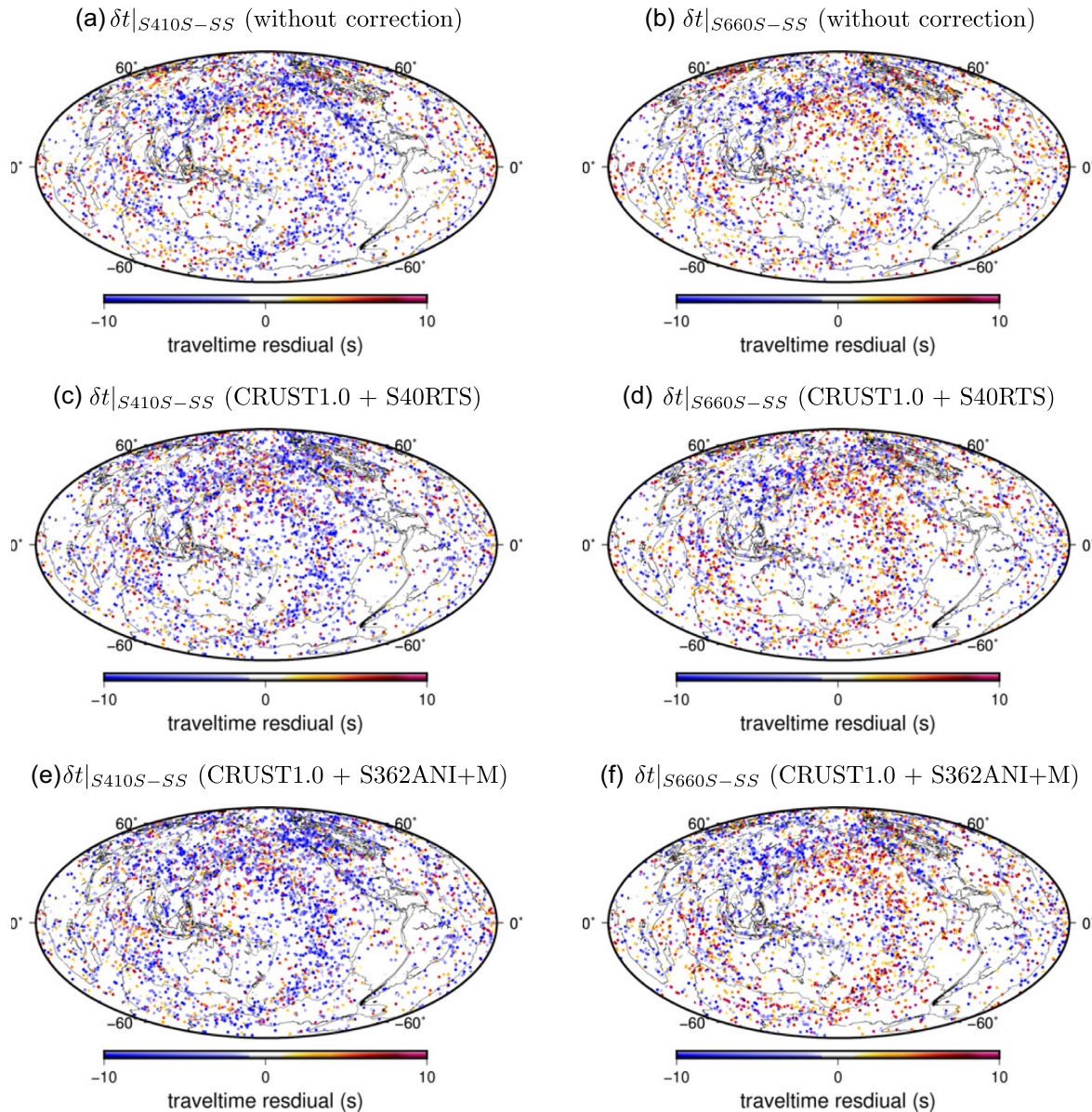


**Figure 9.** Panels (a) and (b) are  $S_{410S-SS}$  and  $S_{660S-SS}$  differential traveltime measurements at a period of 20 s without crustal and mantle corrections. The measurements are plotted at the bounce points of SS waves. Panels (c) and (d) are the same as (a) and (b) but with data corrected for crustal and mantle wave speed variations using models CRUST1.0 and S40RTS. (e) and (f) are the same as (c) and (d) but with mantle corrections using model S362ANI+M.

correlated regardless of the 3-D wave speed model used in making the corrections.

## 7 DISCONTINUITY TOPOGRAPHY AND WAVE SPEED STRUCTURE

The Clapeyron slope, which is the change in pressure over the change in temperature  $dP/dT$ , is positive for the olivine to wadsleyite phase transformation (the 410-km discontinuity) and negative for the ringwoodite to perovskite and magnesiowüstite phase transformation (the 660-km discontinuity). If undulations of the two discontinuities are dominantly caused by lateral thermal variations in the mantle transition zone, we would expect a negative correlation between the 410 topography and variations in seismic wave speed. For example, in regions where cold slab materials reside in the mantle transition zone, seismic wave speed

increases while the depth of the 410-km discontinuity decreases, resulting in a negative correlation. In contrast, the correlation between wave speed and discontinuity depth would be positive for the 660-km discontinuity due to its opposite Clapeyron. Examining the correlations between perturbations in wave speed and discontinuity depth will in turn allow us to investigate dominant mechanisms responsible for depth perturbations of the 410- and 660-km discontinuities.

In Fig. 12, we investigate the correlation between discontinuity depth perturbations and seismic wave speed variations in the mantle transition zone using a global model S40RTS (Ritsema *et al.* 2011). The discontinuity models are obtained from traveltime data with corrections made using the same wave speed model. There is no clear correlation between the topography of the 410-km discontinuity and wave speed variations at a global scale, except for at spherical harmonics degree  $l = 4$  (length scale of  $\sim 5000$  km) where

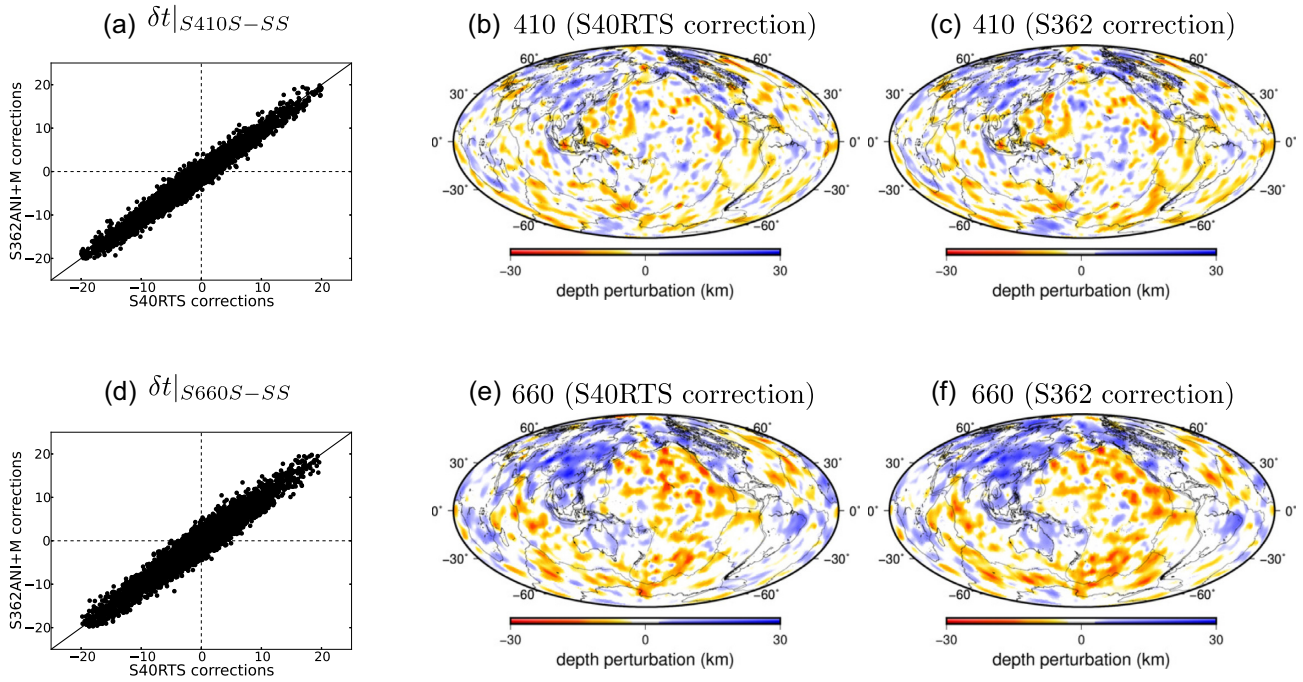


**Figure 10.** (a) Scatterplot of  $S_{410S-SS}$  differential traveltime measurements with mantle corrections made using model S40RTS (Ritsema *et al.* 2011) and model S362ANI+M (Moulik & Ekstrom 2014). Panels (b) and (c) are depth perturbations of the 410-km discontinuity from finite-frequency tomography with traveltime corrections made using model S40RTS and S362ANI+M, respectively. Panels (d)–(f) are the same as (a)–(c) but for the 660-km discontinuity.

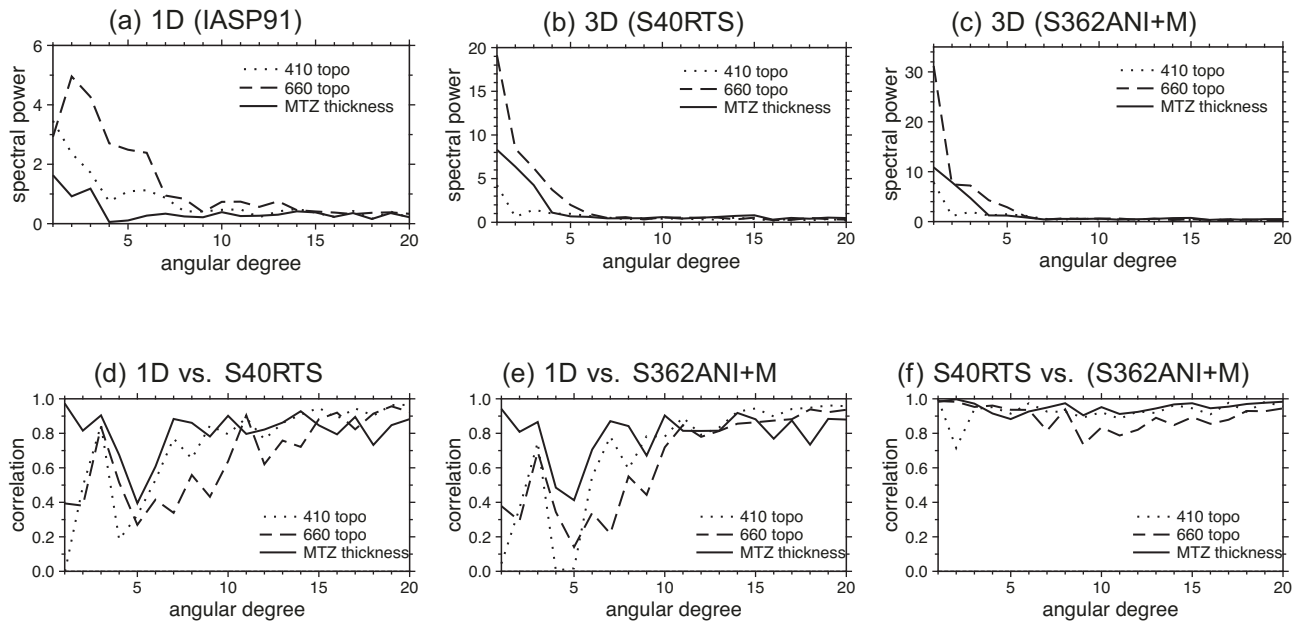


**Figure 11.** (a) Spectra power per spherical harmonic degree of the finite-frequency 410- and 660-km discontinuity models in Fig. 6 and the corresponding mantle transition zone thickness. (b) and (c) are the same as (a) but for discontinuity models in Fig. 10 where traveltime corrections have been made using model S40RTS and S362ANI+M, respectively. (d) Correlation coefficients as a function of spherical harmonic degree between the discontinuity models obtained with and without corrections based on model S40RTS (Figs 6 and 10). (e) is the same as (d) for models with and without traveltime corrections made using model S362ANI+M. Panel (f) correlation coefficients between models obtained with corrections made using models S40RTS and S362ANI+M.

the correlation is positive. The absence of an overall negative correlation between seismic wave speed and the 410-km discontinuity suggests possible non-thermal origin of heterogeneities. For example, heterogeneities in chemical composition or changes in water content (Schmerr & Garnero 2007; Gu *et al.* 2014; Wang *et al.* 2017).

The topography of the 660-km discontinuity, on the other hand, shows clear positive correlations with seismic wave speed in the mantle transition zone up to spherical harmonic degree  $l = 11$  (length scale of  $\sim 3600$  km). This positive correlation supports a thermal origin at a global scale. The correlation becomes weaker at higher spherical harmonic degrees and no apparent correlation

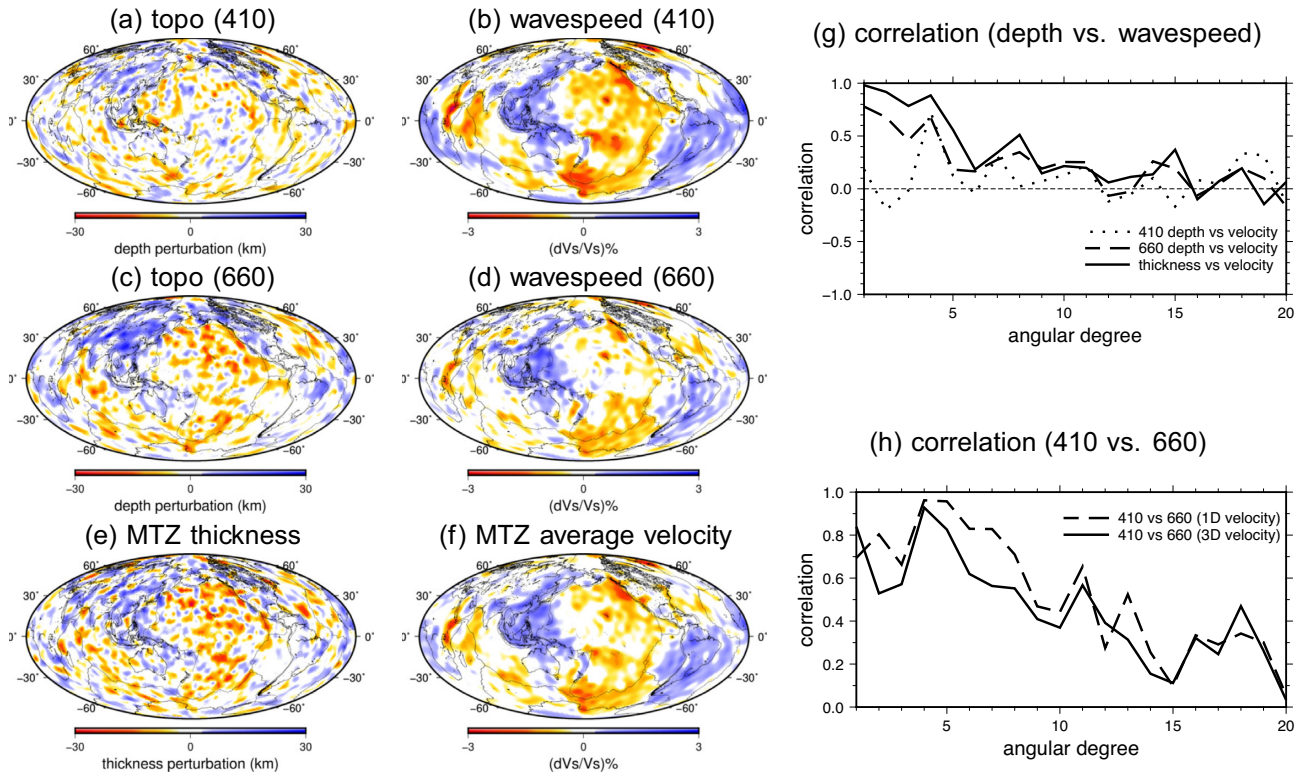


**Figure 12.** Panels (a) and (c) are the finite-frequency 410- and 660-km discontinuity models with data corrections made using model S40RTS (Fig. 10). Panels (b) and (d) are wave speed perturbations in model S40RTS at depths of 410 and 660 km, respectively. Panels (e) and (f) are maps of the mantle transition zone thickness and average wave speed in the mantle transition zone, respectively. Panel (g) correlation between discontinuity depth perturbations and wave speed perturbations as a function of spherical harmonic degree; (h) correlation between the 410- and 660-km discontinuity models in 1-D (no correction) and 3-D (with correction) wave speed models.

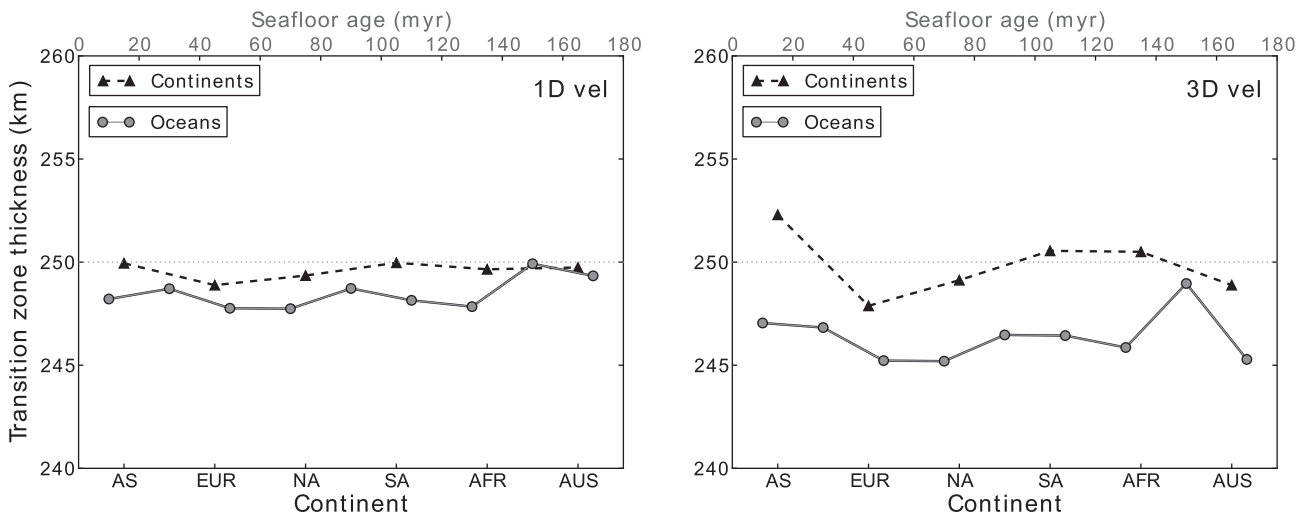


**Figure 13.** Average mantle transition zone thickness in 1-D (left-hand panel) and 3-D (right-hand panel) wave speed models. In the oceans, the thickness is averaged over every 20-Myr age band and there is no apparent dependence on the age of the sea floor. The average thickness of the mantle transition zone in continental areas is calculated for Asia (AS), Europe (EUR), North America (NA), South America (SA), Africa (AFR) and Australia (AUS). The mantle transition zone is thicker under the continents than under the oceans, especially after crustal and wave speed corrections are applied.

is observed at  $l > 15$  (lengthscale  $\sim 1300$  km), which is likely due to different lateral resolutions in the wave speed and topography models. This change from no (weak) correlation at 410 km depth to significant positive correlation at 660 km depth may also be a result of limitations in depth resolution of the global seismic wave speed model over a scale of 250 km in the mantle transition zone.

The thickness of the mantle transition zone shows strongest correlation with seismic wave speed. This positive correlation is not surprising as variations in thickness are dominated by the depth perturbations on the 660-km discontinuity, and, there is a positive correlation between the 660-km discontinuity topography and seismic wave speed. The correlation is stronger in long wavelength

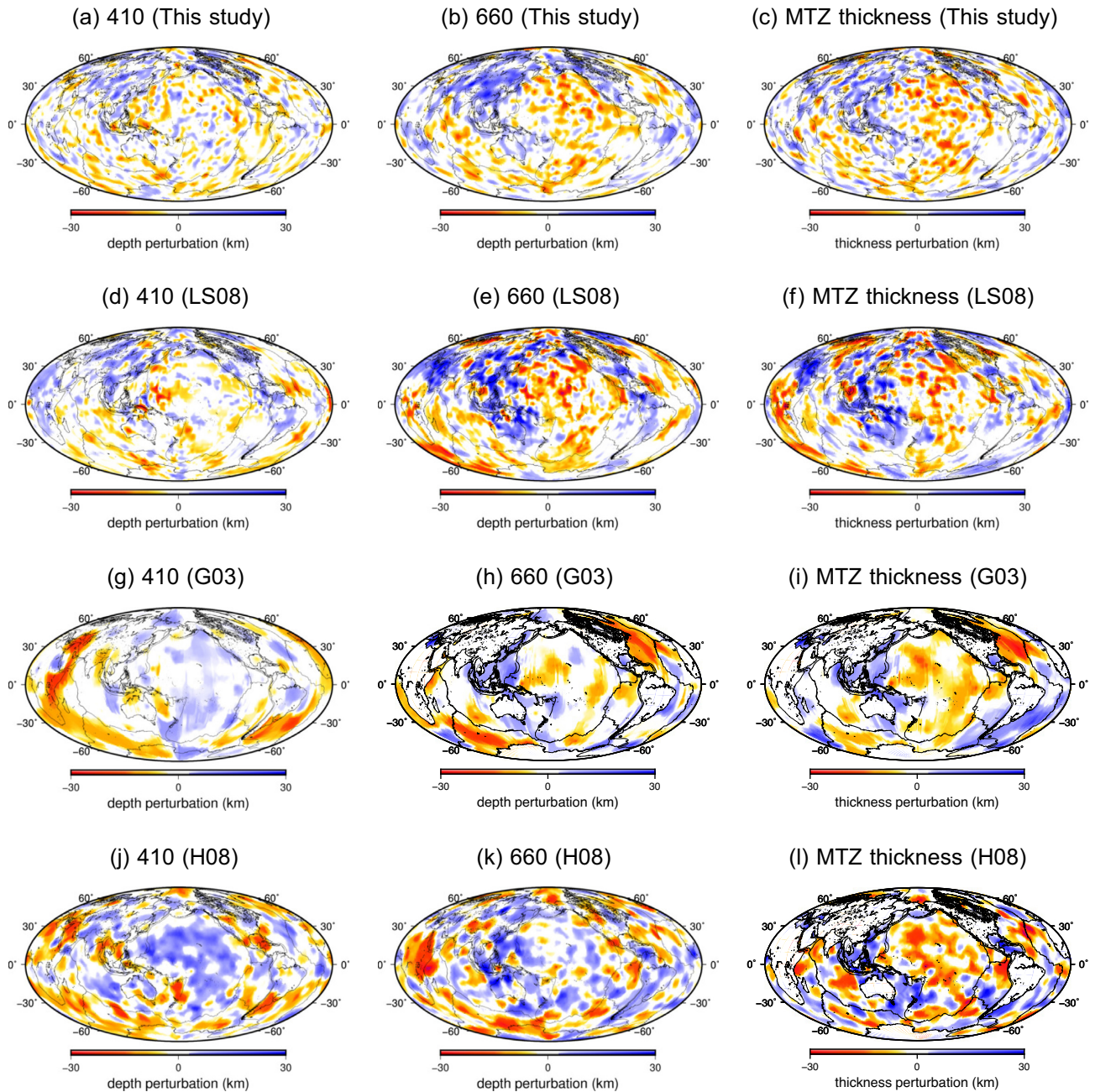


**Figure 14.** This figure compares the topography of the 410- and 660-km discontinuity as well as the thickness of the mantle transition zone from (a)–(c) this study, (d)–(f) Lawrence & Shearer (2008), (g)–(i) Gu *et al.* (2003) and (j)–(l) Houser *et al.* (2008).

variations at spherical harmonic degree  $l < 8$ . Geographically, the mantle transition zone is thicker beneath the Pacific subduction zones and thinner beneath the oceans, consistent with previous studies (Flanagan & Shearer 1998; Gu *et al.* 1998, 2003).

In Fig. 13, we plot the average thickness of the mantle transition zone beneath continental areas in Asia, Europe, North America, South America, Africa and Australia. The average thickness of the mantle transition zone beneath continental areas is overall very close to that in the reference model (250 km). Crustal and mantle wave speed corrections have little impact on the mantle transition zone thickness except for in Asia, Europe and Australia. The corrections result in a 2.3-km-thicker mantle transition zone beneath Asia and 1.0 and 0.9 km thinner mantle transition zone beneath Europe and

Australia, respectively. In oceanic regions, the mantle transition zone is about 1.5 km thinner than the reference model and the amount of the thinning increases to 4.6 km when CRUST1.0 and model S40RTS are applied to make traveltime corrections. There is no obvious correlation between the thickness of the mantle transition zone and the age of the seafloor.

## 8 COMPARISON WITH PREVIOUS GLOBAL MODELS

In Fig. 14, we compare the 410- and 660-km discontinuity models in this study with three recent global models imaged based on SS waves and their precursors: Gu *et al.* (2003), Houser *et al.* (2008)

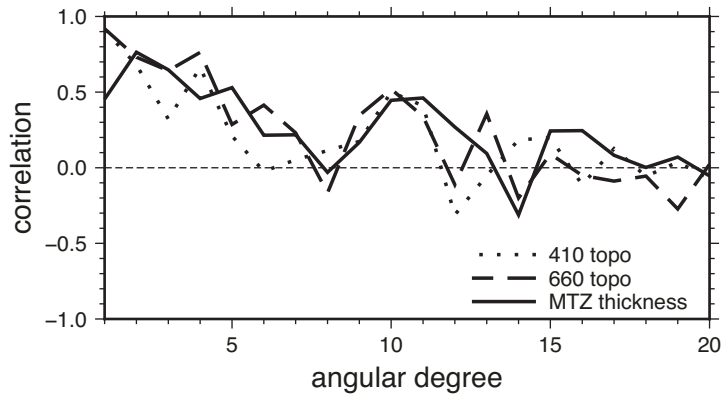


**Figure 15.** Correlation between discontinuity models in this study and model LS08 (Lawrence & Shearer 2008). The coefficients are plotted as a function of spherical harmonic degree from 1 to 20 for depth perturbations on the 410-km discontinuity, the 660-km discontinuity and the thickness of the mantle transition zone.

and Lawrence & Shearer (2008). The four 660-km discontinuity models all show some consistent features. In particular, along subduction zones in the Western Pacific, the 660-km discontinuity is overall deeper than the global average. The mantle transition zone is thicker in the Western Pacific and thinner in the Pacific Ocean. However, large discrepancies exist in the Pacific Ocean. The most extreme disagreement appears to be structures on the 410-km discontinuity maps. For example, the strong depression of the 410-km discontinuity in the Pacific Ocean in Model H08 (Houser *et al.* 2008) is either absent or much weaker in the other models. The broad uplift of the 660-km discontinuity in the northern Atlantic Ocean in model Model G03 Gu *et al.* (2003) is weak (absent) in other models. At regional scales, the discrepancies involve reversed polarities in western North America and southeast Asia.

Among all global models, the 410- and 660-km discontinuity depth perturbations obtained from this study agree best with the finite-frequency model published by Lawrence & Shearer (2008) (Model LS08). In Fig. 15, we plot the correlation coefficients between the two models as a function of spherical harmonic degree. The long-wavelength structures in the 660-km discontinuity depth perturbations between the two models are in good agreement, with a positive correlation of  $\sim 0.76$  at spherical harmonic degrees  $l \leq 4$ . The correlations are only slightly weaker for the 410-km discontinuity with a correlation coefficient of  $\sim 0.64$ . Significant discrepancies can be observed in their smaller scale features. For example, the 410-km discontinuity models filtered at spherical harmonic degrees  $l \leq 6$  starts to show major differences in the Pacific Ocean (Fig. 16), and the correlation coefficient between the two models decreases to  $\sim 0.1$  at  $l = 5-7$ . At spherical harmonic degree  $l \leq 12$ , the 410-km discontinuity is depressed beneath the Red Sea in our model which is absent in model LS08. A strong negative anomaly in the 410-km discontinuity along the southeast Indian ridge into the southern Atlantic Ocean in model LS08 is absent (much weaker) in our model. Major discrepancies on the 660-km discontinuity include a strong depression beneath the Arabian Plate and the Mediterranean sea in model LS08 and a broad uplift in the Northwest Pacific beneath the old Pacific Plate, which are absent in our model as well as in the other two models (Fig. A2). Overall, the correlations between the new discontinuity model and model LS08 decreases with spherical harmonic degree and there is no apparent correlation between the two models at degree  $l > 15$ .

The fact that the general features in the Lawrence & Shearer (2008) model agree better with this study than other ray-theoretical models is somewhat expected as both studies are based on tomographic inversions using finite-frequency sensitivity kernels. The sensitivity kernels in Lawrence & Shearer (2008) were calculated based on ray tracing, which is computationally efficient but the sensitivity kernels do not account for phase interactions and windowing/tapering applied in seismograms. However, it is noteworthy that differences between our finite-frequency models and back-projection models obtained using the exact same data set are less significant than that between the two finite-frequency models. This reflects the importance of using complete finite-frequency sensitivities in data selection and processing. For example, measurements associated with very complex or extreme sensitivity to depth perturbations of the two discontinuities should be excluded.

## 9 CONCLUSIONS

In this paper, we investigate the finite-frequency effects in imaging the global structure of the 410- and 660-km discontinuities using *SdS* precursors. The finite-frequency *SdS*–*SS* traveltimes measurements are made using seismograms recorded at GSN stations for earthquakes occurred between 2003 and 2014. The finite-frequency traveltimes differences between observed and synthetic seismograms are measured in the frequency domain using a cosine taper. The sensitivity kernels for *SS* waves and precursors are calculated in the framework of travelling-wave mode coupling, and fully accounts for phase interactions within the measurement window.

The finite-frequency models correlated well with ray-theoretical back-projection models in their large scale structure but the finite-frequency models show much stronger small-scale features when the smoothness (coverage) of the back-projection ray density are comparable to that of the finite-frequency sensitivity density. Crustal and mantle wave speed corrections do not change the general geographic pattern of the *SdS*–*SS* traveltimes measurements and discontinuity models inverted with and without crustal and mantle corrections are overall well correlated, regardless of the global wave speed models used in making the corrections.

The finite-frequency 660-km discontinuity model is overall positively correlated with wave speed perturbations in the mantle transition zone, indicating a dominant thermal origin for depth perturbations of the 660-km discontinuity. However, a clear correlation

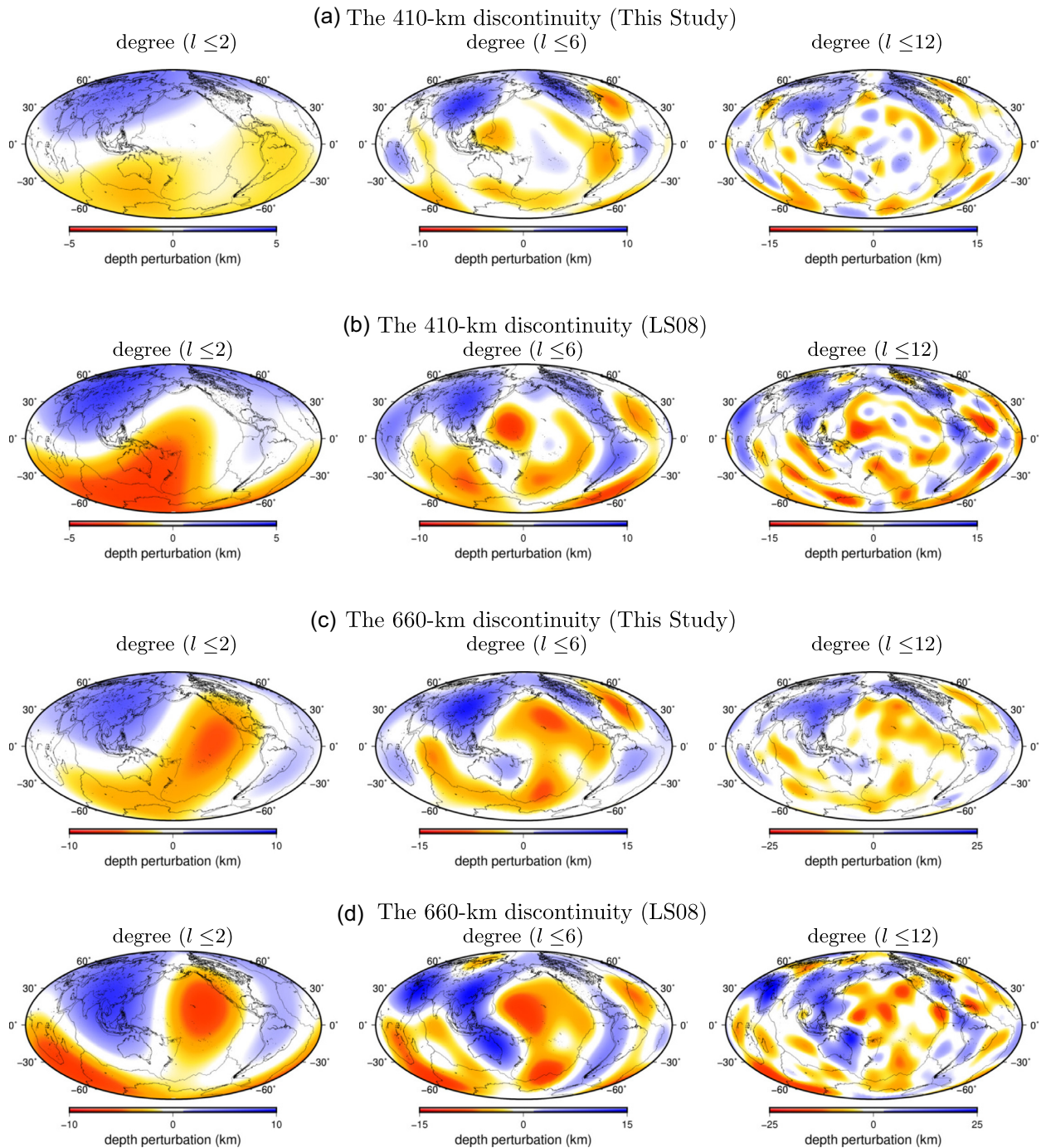


**Figure 16.** Panel (a) is the 410-km discontinuity model in this study filtered to spherical harmonic  $l \leq 2$ ,  $l \leq 6$  and  $l \leq 12$ . Panel (b) is the same as (a) but for the 410-km discontinuity model from Lawrence & Shearer (2008), panels (c) and (d) are the same as (a) and (b) but for the 660-km discontinuity.

between the 410-km discontinuity and seismic wave speed is not observed, which suggests possible non-thermal heterogeneities in the upper mantle transition zone or limited vertical resolution in seismic wave speed tomography. We compare global mantle transition zone discontinuity models obtained from *SS* precursors and show that our finite-frequency model agrees best with the model of Lawrence & Shearer (2008), which is also a finite-frequency model but with sensitivities calculated based on ray tracing and additional kernel stacking. However, major discrepancies exist between the two models in both oceanic regions and subduction zones, suggesting the significance of wave interference in the calculations of

sensitivity kernels as well as the use of finite-frequency sensitivities in data quality control. For example, measurements associated with very complex or extreme sensitivity to discontinuity depth perturbations can be identified in travelling-wave mode coupling and those measurements can be excluded from tomographic inversions.

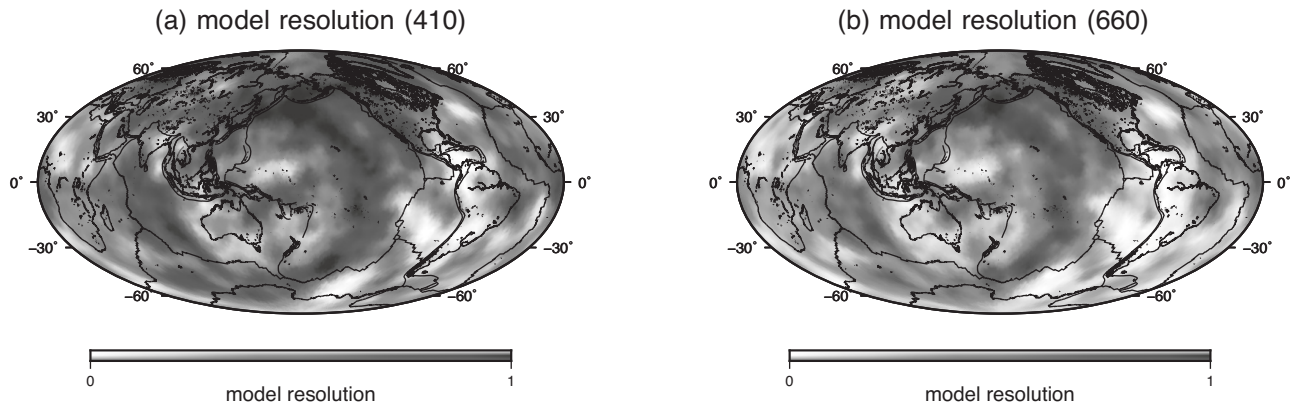
## ACKNOWLEDGEMENTS

We thank Dr Daniel A Frost and an anonymous reviewer for their constructive comments and Editor Ian Bastow for his professional

handling of the manuscript. The facilities of the IRIS Data Management System, and specifically the IRIS Data Management Center, were used for access to waveform and metadata required in this study. The authors acknowledge Advanced Research Computing at Virginia Tech for providing computational resources and technical support. This research was supported by the U.S. National Science Foundation under Grants EAR-1737737. All figures were generated using the Generic Mapping Tools (GMT) (Wessel & Smith 1995).

## REFERENCES

- Anderson, D.L., 1967. Phase changes in the upper mantle, *Science*, **157**, 1165–1173.
- Chevrot, S., Vinnik, L. & Montagner, J.-P., 1999. Global-scale analysis of the mantle Pds phases, *J. geophys. Res.*, **104**, 20203–20219.
- Dahlen, F., 2005. Finite-frequency sensitivity kernels for boundary topography perturbations, *Geophys. J. Int.*, **162**, 525–540.
- Deng, K. & Zhou, Y., 2015. Wave diffraction and resolution of mantle transition zone discontinuities in receiver function imaging, *Geophys. J. Int.*, **201**, 2008–2025.
- Deuss, A., 2009. Global observations of mantle discontinuities using SS and PP precursors, *Surv. Geophys.*, **30**, 301–326.
- Dziewonski, A. & Anderson, D., 1981. Preliminary reference earth model, *Phys. Earth planet. Inter.*, **25**, 297–356.
- Flanagan, M. & Shearer, P., 1998. Global mapping of topography on transition zone discontinuities by stacking of SS precursors, *J. geophys. Res.*, **103**, 2673–2692.
- Gao, S.S. & Liu, K.H., 2014. Mantle transition zone discontinuities beneath the contiguous United States, *J. geophys. Res.*, **119**, 6452–6468.
- Gu, Y., Dziewonski, A. & Agee, C., 1998. Global de-correlation of the topography of transition zone discontinuities, *Earth planet. Sci. Lett.*, **157**, 57–67.
- Gu, Y., Dziewonski, A. & Ekstrom, G., 2003. Simultaneous inversion for mantle shear velocity and topography of transition zone discontinuities, *Geophys. J. Int.*, **154**, 559–583.
- Gu, Y.J. & Dziewonski, A.M., 2002. Global variability of transition zone thickness, *J. geophys. Res.*, **107**, doi:10.1029/2001JB000489.
- Gu, Y.J., Zhang, Y., Sacchi, M.D., Chen, Y. & Contenti, S., 2014. Sharp mantle transition from Cratons to Cordillera in southwestern Canada, *J. geophys. Res.*, **120**, 5051–5069.
- Heit, B., Yuan, X., Bianchi, M., Kind, R. & Gossler, J., 2010. Study of the lithospheric and upper-mantle discontinuities beneath eastern Asia by SS precursors, *Geophys. J. Int.*, **183**, 252–266.
- Houser, C., Masters, G., Flanagan, M. & Shearer, P., 2008. Determination and analysis of long-wavelength transition zone structure using SS precursors, *Geophys. J. Int.*, **174**, 178–194.
- Ita, J. & Stixrude, L., 1992. Petrology, elasticity, and composition of the mantle transition zone, *J. geophys. Res.*, **97**, 6849–6866.
- Kavianian, A., Sandvol, E., Moradi, A., Rumpker, G., Tang, Z. & Mai, P.M., 2018. Mantle transition zone thickness beneath the Middle East: evidence for segmented Tethyan slabs, delaminated lithosphere, and lower mantle upwelling, *J. geophys. Res.*, **123**, 4886–4905.
- Kennett, B.L.N. & Engdahl, E.R., 1991. Traveltimes for global earthquake location and phase identification, *Geophys. J. Int.*, **105**, 429–465.
- Kosarev, G., Oreshin, S., Vinnik, L. & Makeyeva, L., 2017. Mantle transition zone beneath the central Tien Shan: Lithospheric delamination and mantle plumes, *Tectonophysics*, **723**, 172–177.
- Kustowski, B., Ekstrom, G. & Dziewonski, A., 2008. Anisotropic shear-wave velocity structure of the Earth's mantle: A global mode, *J. geophys. Res.*, **113**, doi:10.1029/2007JB005169.
- Laske, G., Masters, G., Ma, Z. & Pasyanos, M., 2013. Update on CRUST1.0—a 1-degree global model of Earth's crust, *EGU General Assembly Conference Abstracts*, **15**, 2658.
- Lawrence, J. & Shearer, P., 2006. A global study of transition zone thickness using receiver functions, *J. geophys. Res.*, **111**, doi:10.1029/2005JB003973.
- Lawrence, J.F. & Shearer, P.M., 2008. Imaging mantle transition zone thickness with SdS-SS finite-frequency sensitivity kernels, *Geophys. J. Int.*, **174**, 143–158.
- Lee, S.-H., Rhie, J., Park, Y. & Kim, K.-H., 2014. Topography of the 410 and 660 km discontinuities beneath the Korean peninsula and southwestern Japan using teleseismic receiver functions, *J. geophys. Res.*, **119**, 7245–7257.
- Lessing, S., Thomas, C., Rost, S., Cobden, L. & Dobson, D.P., 2014. Mantle transition zone structure beneath India and western China from migration of PP and SS precursors, *Geophys. J. Int.*, **197**, 396–413.
- Li, X. & Yuan, X., 2003. Receiver functions in northeast China - implications for slab penetration into the lower mantle in northwest Pacific subduction zone, *Earth planet. Sci. Lett.*, **216**, 679–691.
- Liu, K. & Zhou, Y., 2016. Travelling-wave green tensor and near-field Rayleigh-wave sensitivity, *Geophys. J. Int.*, **205**, 134–145.
- Moulik, P. & Ekstrom, G., 2014. An anisotropic shear velocity model of the earth's mantle using normal modes, body waves, surface waves and long-period waveforms, *Geophys. J. Int.*, **199**, 1713–1738.
- Neele, F. & de Regt, H., 1999. Imaging upper-mantle discontinuity topography using underside-reflection data, *Geophys. J. Int.*, **137**, 91–106.
- Neele, F., de Regt, H. & VanDecar, J., 1997. Gross errors in upper-mantle discontinuity topography from underside reflection data, *Geophys. J. Int.*, **129**, 194–204.
- Panning, M. & Romanowicz, B., 2006. A three-dimensional radially anisotropic model of shear velocity in the whole mantle, *Geophys. J. Int.*, **167**, 361–379.
- Revenaugh, J. & Jordan, T.H., 1991. Mantle layering from ScS reverberations: the transition zone, *J. geophys. Res.*, **96**, 19 763–19 780.
- Ritsema, J., Deuss, A., van Heijst, H. & Woodhouse, J., 2011. S40rts: a degree-40 shear-velocity model for the mantle from new Rayleigh wave dispersion, teleseismic traveltime and normal-mode splitting function measurements, *Geophys. J. Int.*, **184**, 1223–1236.
- Schaeffer, A. & Levedev, S., 2013. Global shear speed structure of the upper mantle and transition zone, *Geophys. J. Int.*, **194**, 417–449.
- Schmerr, N. & Garnero, E., 2006. Investigation of upper mantle discontinuity structure beneath the central Pacific using SS precursors, *J. geophys. Res.*, **111**, doi:10.1029/2005JB004197.
- Schmerr, N. & Garnero, E.J., 2007. Upper mantle discontinuity topography from thermal and chemical heterogeneity, *Science*, **318**, 623–626.
- Schmerr, N. & Thomas, C., 2011. Subducted lithosphere beneath the Kuriles from migration of PP precursors, *Earth planet. Sci. Lett.*, **311**, 101–111.
- Shearer, P.M., 1991. Constraints on upper mantle discontinuities from observations of long-period reflected and converted phases, *J. geophys. Res.*, **96**, 18 147–18 182.
- Shen, Y., Sheehan, A.F., Dueker, K.G., de Groot-Hedlin, C. & Gilbert, H., 1998. Mantle discontinuity structure beneath the southern East Pacific Rise from P-to-S converted phases, *Science*, **280**(5367), 1232–1235.
- Wang, X., Li, J. & Chen, Q.-F., 2017. Topography of the 410 km and 660 km discontinuities beneath the Japan Sea and adjacent regions by analysis of multiple-ScS waves, *J. geophys. Res.*, **122**, 1264–1283.
- Wang, Y. & Pavlis, G.L., 2016. Roughness of the mantle transition zone discontinuities revealed by high-resolution wavefield imaging, *J. geophys. Res.*, **121**, doi:10.1002/2016JB013205.
- Wessel, P. & Smith, W.H.F., 1995. New version of the generic mapping tools released, *EOS, Trans. Am. geophys. Un.*, **76**, 329.
- Xue, J., Chen, Y. & Zhou, Y., 2015. Tomographic resolution of plume anomalies in the lowermost mantle, *Geophys. J. Int.*, **201**, 979–995.
- Zheng, Z., Ventosa, S. & Romanowicz, B., 2015. High resolution upper mantle discontinuity images across the Pacific Ocean from SS precursors using local slant stack filters, *Geophys. J. Int.*, **202**, 175–189.
- Zhou, Y., 2009. Multimode surface wave sensitivity kernels in radially anisotropic earth media, *Geophys. J. Int.*, **176**, 865–888.
- Zhou, Y., 2018. Anomalous mantle transition zone beneath the Yellowstone hotspot track, *Nat. Geosci.*, **11**, 449–453.
- Zhou, Y., Dahlen, F.A., Nolet, G. & Laske, G., 2005. Finite-frequency effects in global surface-wave tomography, *Geophys. J. Int.*, **163**, 1087–1111.
- Zhou, Y., Nolet, G., Dahlen, F.A. & Laske, G., 2006. Global upper-mantle structure from finite-frequency surface-wave tomography, *J. geophys. Res.*, **111**, doi:10.1029/2005JB003677.

APPENDIX: MODEL RESOLUTION AND  
ADDITIONAL MODEL COMPARISON

**Figure A1.** Panels (a) and (b) show the resolution of the finite-frequency 410- and 660-km discontinuity models obtained in this study, plotted in every  $4^\circ \times 4^\circ$  grid cell based on diagonal elements of the resolution matrices. In regions where the diagonal elements of the resolution matrix are close to 1, discontinuity depth perturbations are well recovered. The difference between the recovered model and the true model  $\mathbf{x} - \mathbf{x}_{\text{true}} = (\mathbf{R} - \mathbf{I})\mathbf{x}_{\text{true}}$  depends on the resolution matrix  $\mathbf{R}$  as well as the earth structure  $\mathbf{x}_{\text{true}}$ . For example, in a region where the diagonal element of the resolution matrix is 0.9 and the true depth perturbation is 10 km, the uncertainty due to lack of resolution is about 1 km.

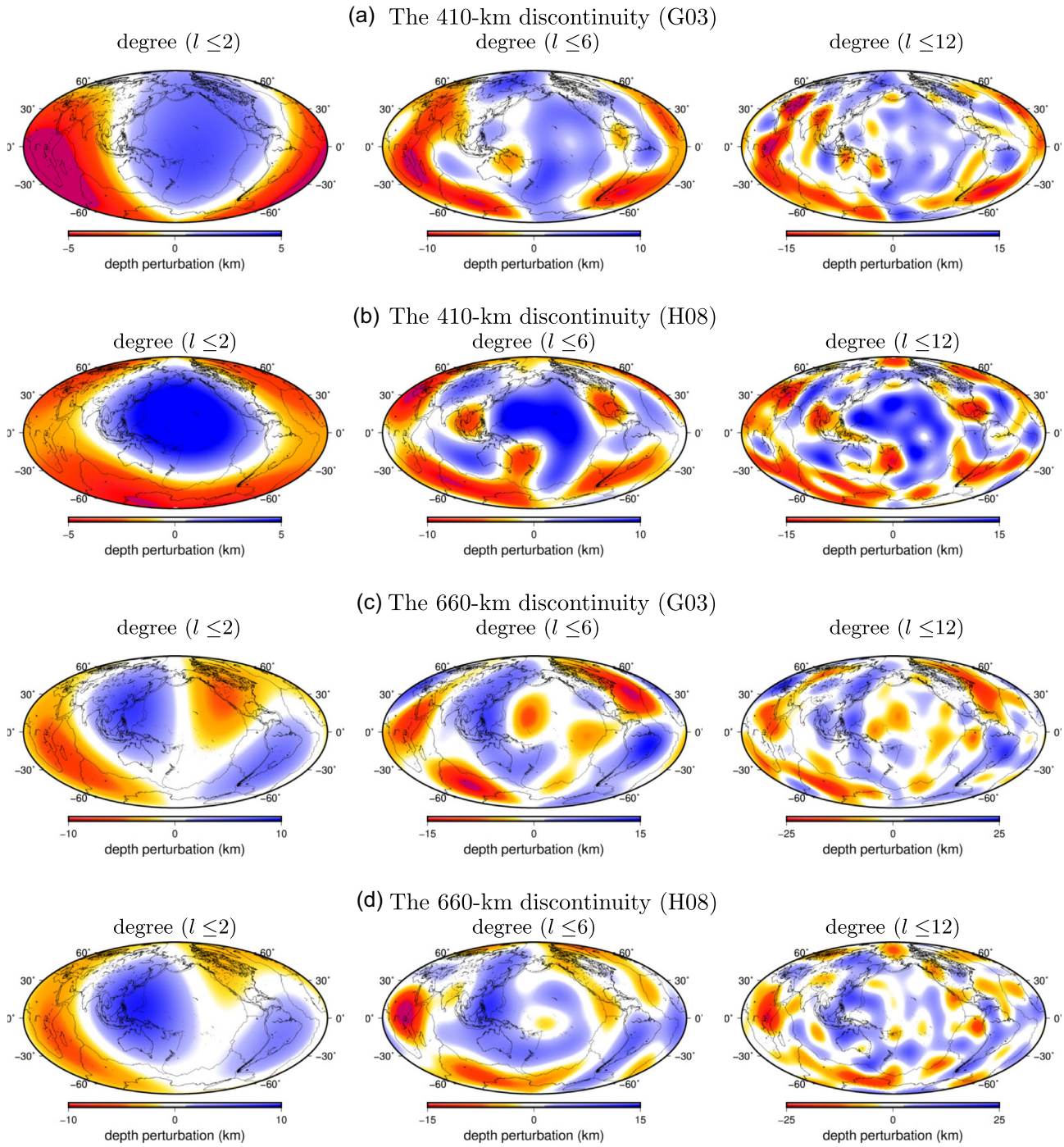


Figure A2. Same as Fig. 16 but for models from Gu *et al.* (2003) and Houser *et al.* (2008).